

Diagenetic silica enrichment and late-stage groundwater activity in Gale crater, Mars

J. Frydenvang^{1,2}, P.J. Gasda¹, J.A. Hurowitz³, J.P. Grotzinger⁴, R.C. Wiens¹, H.E. Newsom⁵, K.S. Edgett⁶, J. Watkins⁴, J.C. Bridges⁷, S. Maurice⁸, M.R. Fisk⁹, J.R. Johnson¹⁰, W. Rapin⁴, N.T. Stein⁴, S.M. Clegg¹, S.P. Schwenzer¹¹, C.C. Bedford¹¹, P. Edwards⁷, N. Mangold¹², A. Cousin⁸, R.B. Anderson¹³, V. Payré¹⁴, D. Vaniman¹⁵, D.F. Blake¹⁶, N.L. Lanza¹, S. Gupta¹⁷, J. Van Beek⁶, V. Sautter¹⁸, P.-Y. Meslin⁸, M. Rice¹⁹, R. Milliken²⁰, R. Gellert²¹, L. Thompson²², B.C. Clark²³, D.Y. Sumner²⁴, A.A. Fraeman²⁵, K.M. Kinch², M.B. Madsen², I.G. Mitrofanov²⁶, I. Jun²⁵, F. Calef²⁵, A.R. Vasavada²⁵

1. Los Alamos National Laboratory, Los Alamos, NM, USA
2. University of Copenhagen, Copenhagen, Denmark
3. Stony Brook University, Stony Brook, NY, USA
4. California Institute of Technology, Pasadena, CA, USA
5. University of New Mexico, Albuquerque, NM, USA
6. Malin Space Science Systems, San Diego, CA, USA
7. University of Leicester, Leicester, UK
8. L'Institut de Recherche en Astrophysique et Planétologie, Toulouse, France
9. Oregon State University, Corvallis, OR, USA
10. Johns Hopkins University, Laurel, MD, USA
11. Open University, Milton Keynes, UK
12. Université de Nantes, Nantes, France
13. United States Geological Survey, Flagstaff, AZ, USA
14. GeoRessources, Université de Lorraine, Nancy, France
15. Planetary Science Institute, Tucson, AZ, USA
16. NASA Ames Research Center, Moffett Field, CA, USA
17. Imperial College, London, UK
18. IMPMC, Muséum National d'Histoire Naturelle, Paris, France
19. Western Washington University, Bellingham, WA, USA
20. Brown University, Providence, RI, USA
21. University of Guelph, Guelph, ON, Canada
22. University of New Brunswick, Fredericton, New Brunswick, Canada
23. Space Science Institute, Boulder, CO, USA
24. University of California – Davis, Davis, CA, USA
25. Jet Propulsion Laboratory, California Institute of Technology, Pasadena, CA, USA
26. Space Research Institute, Moscow, Russia

Contents of this file

Section 1 - Materials and Methods
Supplementary information text S1
Supplementary information text S2
Figures S1 to S9

Additional Supporting Information (Files uploaded separately)

Supplementary table 1 – ChemCam data
Supplementary table 2 – APXS data

Introduction

Description of data processing for ChemCam and APXS data is provided in **Materials and Methods**. **Supplementary Information A** details the issues observed with the standard ChemCam Ti calibration at the very high silica content targets observed and **Supplementary Information B** details the issues regarding comparison of APXS and ChemCam data-points and causes for the differences observed.

Figures S1 to S9 provides additional information regarding the silica enrichment diagenesis observed in Gale crater, Mars, and the observations acquired by the Mars Science Laboratory Curiosity rover.

Materials and Methods

In total, we collected and studied more than 1200 individual ChemCam [Maurice *et al.*, 2012; Wiens *et al.*, 2012] measurement points and 38 Alpha Particle X-ray Spectrometer (APXS) [Gellert *et al.*, 2015] measurements. Additionally, we acquired and examined hundreds of supporting Mastcam [Malin *et al.*, 2010], Navcam [Maki *et al.*, 2012] and Mars Hand Lens Imager (MAHLI) [Edgett *et al.*, 2012] images were acquired.

ChemCam

ChemCam is a combined remote sensing elemental analysis- and micro imager instrument on the Curiosity rover. Utilizing the technology, Laser-Induced Breakdown Spectroscopy, target compositions are acquired from point-rasters, typically in the form of 1x5, 1x10 line scans or 3x3 grids, at stand-off distances up to 7 m [Maurice *et al.*, 2012; Wiens *et al.*, 2012]. The initial laser pulses at each observation point effectively remove the otherwise ubiquitous dust-cover found on martian targets in the first 5 shots at each point. For this reason, the average spectrum of the 6th to the (typically) 30th shot is utilized to determine the composition of an observation point for the major elements, reported as oxides: SiO₂, Al₂O₃, TiO₂, FeO_T, MgO, CaO, Na₂O and K₂O. See Supplementary Table 1 for all compositions,

All spectra were pre-processed as described by [Wiens *et al.*, 2013]; the oxide composition was calculated as a weighted average between two multivariate models utilizing Partial Least Squares regression (PLS1) and Independent Component Analysis regression (ICA), respectively. The details of the calibration are provided in [Clegg *et al.*, 2017] and also on the ChemCam page of the NASA Planetary Data System archive (<http://pds-geosciences.wustl.edu/missions/msl/chemcam.htm>) where all ChemCam spectra, compositions and images are likewise available.

Classification of ChemCam observation points

Due to the observation footprint of ChemCam (350-550 μm diameter) [Maurice *et al.*, 2012], ChemCam regularly shows measurement-points with a composition that is significantly different from other observation points on the same target. While non-

trivial, these singular points are classified as separate from the general target composition (Supplementary Table S1). Typically, these points are related to diagenetic features such as inclusions of calcium sulfate, but points showing unusually high Al, Fe, Mg or Ti are likewise identified for both Murray and Stimson formation observations. In total, ~10% of all Murray formation observation and ~17% of all Stimson formation observation points were classified as such singular points.

The classification of points as, for example, Murray or Stimson bedrock, float rocks, soil (regolith, eolian sediments), or mixed (combination of 'soil' and bedrock), is based on review of images of the targets and image-based geological mapping. To differentiate between Murray and Stimson rocks, we also found that the potassium content of a given target provided a good discriminator due to its near-constant content in Murray with increasing silica (Supplementary Fig. S7). Finally, points with major-element totals of less than 90% are classified as having low totals.

Definition of high- and low-silica groups, and calculation of added silica

Overall, we studied Murray and Stimson formation rocks at three different, neighboring locations: Marias Pass, Bridger Basin and Williams; the latter covers the rover traverse between Marias Pass and Bridger Basin. To investigate the effect of silica addition, a high- and a low-silica group were identified at each location (only Stimson bedrock was analyzed at Williams). For Murray formation rocks, the low-silica group was defined as the mean composition of the Mission and Piegan targets at Marias Pass, and as the mean composition of the Fisch_Scale target at Bridger Basin. For Stimson formation rocks, due to the larger number of observations on 'baseline' Stimson formation aeolian sandstones, the low-silica composition is defined as the mean composition of all targets with a SiO₂ content below 50 wt.%. For all groups, the high-silica composition is defined as the mean composition of all targets with a silica content above the 80th percentile in silica content for each group individually.

The required volumetric addition of silica to explain the silica content of the highest-silica targets was calculated based on the these high- and low- silica groups. The filling of

pore space by amorphous silica is assumed to provide an increased silica LIBS signal corresponding to the relative volumetric proportion of amorphous silica to bedrock matrix, and not, for example, corresponding to the molar proportion of silica of the bedrock matrix and the added amorphous silica combined. This would imply that more material is ablated when a target is filled with amorphous silica, but we have no way to check this. Based on this assumption, modeled high-silica content is calculated as: $(1-n) \cdot C_{matrix} + n \cdot C_{Si}$, where n is the relative content of amorphous silica, C_{matrix} is the low silica content and C_{Si} represents the content of the amorphous silica – i.e., pure SiO_2 . Here, n is calculated by requiring the modeled high-silica content to match the observed high-silica group; this, in turn permits calculation the modeled content of the other main elements and to compare the results with the observed content.

Passive reflectance

For each ChemCam observation point, a no-laser background (“dark”) spectrum is recorded and subtracted from the active (after laser pulse) spectra as part of the spectral processing. As this spectral processing is performed on Earth, the dark spectrum for every ChemCam observation point is downlinked and available. Based on these, and regular passive observations of known calibration targets on the rover, it is possible to obtain the passive reflectance of each ChemCam observation point. This procedure is described in [Johnson *et al.*, 2015]

APXS

The Alpha Particle X-ray Spectrometer (APXS) is a multiple generation instrument, with previous iterations flown on the NASA Pathfinder and MER rovers. On MSL, APXS has a circular footprint with a diameter of ~ 1.7 cm [Gellert *et al.*, 2015]. The penetration depth varies as a function of element [Rieder *et al.*, 2003], but is typically on the order of tens of micrometers – implying that APXS effectively provides a surface elemental composition measurement.

APXS measurements provide the content of SiO_2 , TiO_2 , Al_2O_3 , FeO , MgO , CaO , Na_2O , K_2O , Cr_2O_3 , MnO , SO_3 , P_2O_5 , Cl , Ni , Zn and Br [Campbell *et al.*, 2012]. APXS

measurements obtained in our study area are provided in Supplementary Table 2. All APXS measurements are available from the APXS page of the NASA PDS archive (<http://pds-geosciences.wustl.edu/missions/msl/apxs.htm>).

Supplementary Information

Text S1: Comparison of ChemCam and APXS measurements of major elements

While both ChemCam and APXS provide elemental compositions, they differ markedly regarding the areal coverage (footprint) of the observations. Where the APXS collects signal from a circular footprint with a diameter of ~1.7 cm [Gellert *et al.*, 2015], the ChemCam footprint is approximately circular with a diameter between 350 μm (2 m stand off) and 550 μm (7 m stand off) [Maurice *et al.*, 2012]. This implies that ChemCam observation points occasionally hit individual mineral grains or thin veins; i.e., *singular* points, that potentially differ substantially from a bulk composition.

Most commonly, such points originate from hitting apparent calcium sulfate veins in the bedrock, yet some points with apparent calcium sulfate do not correspond to veins visible in even the Remote Micro Imager (RMI) that provides detailed context images for each observation point. Such minor calcium sulfate observations might correspond to laser pulses hitting a calcium sulfate intergranular cement [Newsom *et al.*, 2017]. Generally, visible/larger veins are more ubiquitous in the Murray formation relative to Stimson, whereas the thinner/less visible veins are typically observed in Stimson. Apart from points with elevated CaSO_4 , other singular points show strongly elevated Al, Fe, Ti or Mg. In investigating the bedrock composition in Murray and Stimson across the three locations, these singular points were excluded from our ChemCam analysis because these would skew the mean compositions.

Furthermore, APXS and ChemCam differ in how they are affected by the ubiquitous dust coatings found on Mars. APXS collects a surface observation (penetration depth depends on individual elements but on the order of tens of micrometers [Rieder *et al.*, 2003]), and thus provides a weighted mean composition over that surface – including the effects of any dust coating on that surface.

The Curiosity rover is equipped with a brush (DRT) to remove surface dust, but this was not applied to all APXS observations in the study area. Furthermore, a number of APXS measurements were made on drill holes, drill cuttings and drill sample discard piles where the otherwise ubiquitous dust cover (observed in the first few shots of essentially all ChemCam observations) is not present. Plotting APXS measurements of the initial surface DRT measurement of the three drills performed, along with the subsequent associated drill cuttings measurement, it is evident that the DRT-measurements in many instances trend towards the soil composition observed on Mars (here represented by the ‘Portage’ soil observation at the Rocknest location in Gale) relative to the composition observed in the associated drill cuttings observation (Supplementary Fig. S9). This effect is particularly clear for MgO, but also has a marked effect on SiO_2 . The Big_Sky observations show a constant MgO composition for both the DRT and drill cuttings measurements that both approximately match the MgO composition of typical soil. In contrast, a marked drop in MgO is observed for the drill tailings measurements (~1.5 wt.%) of both Buckskin and Greenhorn, relative to the associated DRT measurements (~5 wt.%) – with the DRT measurements trending strongly towards a typical Mars soil MgO composition. A similar trend of the DRT-composition trending towards that of typical Mars soils (being either greater or smaller than that of the associated drill tailings measurement) is observed for

several other elements (e.g. SiO_2 , TiO_2 , Al_2O_3 , K_2O). While it is evident that the measured APXS composition generally provides the composition of the underlying bedrock to good precision, the effects of dust coatings must be taken into consideration.

Text S2: ChemCam issue with Ti-calibration in high-silica matrix

For the high-silica Murray and Stimson bedrock observations, the standard ChemCam calibration provided apparent erroneous – very high – TiO₂ contents relative to what was observed with APXS. In addition to the calculated composition, it was apparent from the spectra that the Ti spectral lines became very dependent on how the spectral lines were normalized.

Normally, spectra are normalized by the total intensity in one of two ways: either by the sum of all spectral channels of all three spectrometers, or the spectrum from each spectrometer is normalized separately by the total intensity of that spectrometer. The strongest diagnostic Ti lines are in the lowest wavelength spectrometer (ultraviolet, UV) of the ChemCam instrument, and so are a large number of Fe lines. This combination is believed to be the reason for the Ti issues observed for the high-silica targets. Specifically, for the diagnostic Ti lines at 365–367nm, it was evident that normalizing the Ti lines in the usual way introduced a positive correlation with increasing silica (and strongly decreasing iron) that was not observed in un-normalized spectra. While normalization is typically required to correct for differences in plasma temperature, ablated material, and etc., it should not introduce correlations that are not observed in the raw data. Normalizing the Ti lines by the total intensity of a different spectrometer (visible/near-infrared, VNIR) without the numerous Fe-lines present in the UV range, did not recreate the erroneous trend introduced by the UV normalization, further corroborating that the very high Ti-content acquired from the standard calibration model was negatively affected by normalization for the very high silica targets.

Specifically, the likely cause for the erroneous high-Ti readings are not the high Si content by itself, but rather the strong negative correlation between Si and Fe. This implies that as silica increases, the iron-content decreases, and given the dominance of Fe-lines on the total intensity of both the UV and all three spectrometers, this caused an increase in the normalized intensity of Ti lines, despite these not increasing in the un-normalized spectra.

This specific effect was not observed in the calibration database used for the ChemCam calibration model, as no calibration samples with high silica (>60 wt.%) displayed a simultaneous TiO₂ content above ~1 wt.%. APXS observed a SiO₂ content ~75 wt.% and TiO₂ content ~1.6 wt.% for the Murray bedrock at Marias Pass. Hence, the Murray bedrock Ti-content is effectively outside the range of the multivariate models used for the ChemCam Ti calibration. For this reason, the un-normalized diagnostic Ti lines (365–367 nm) are used as a qualitative measure of the Ti-content.

Supplementary figures

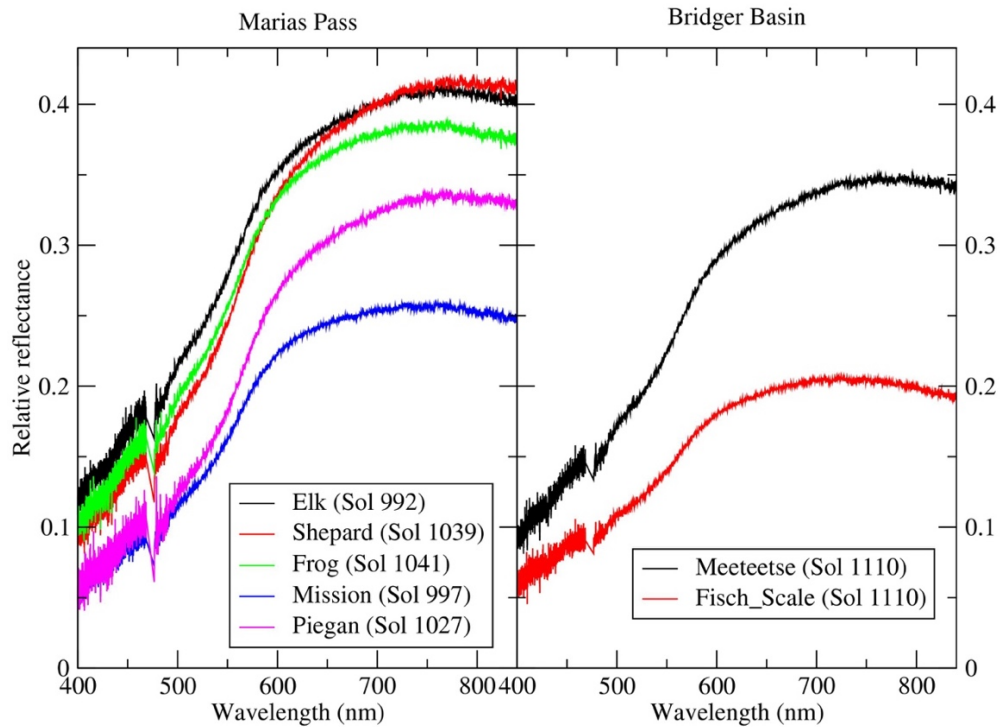


Figure S1: Relative reflectance of individual targets at Marias Pass and Bridger Basin as measured by ChemCam. Target names Elk, Shepard, and Frog represent the highest silica targets observed at Marias Pass, whereas targets Mission and Piegan represent the lowest silica and highest iron targets. A similar chemical variation is observed at Bridger Basin where the target named Meeteetse was a high-silica target and Fisch_Scale was a low-silica, higher-iron target. Overall, the targets at Bridger Basin are slightly darker over the visible/near-IR wavelength region than the comparable targets at Marias Pass.

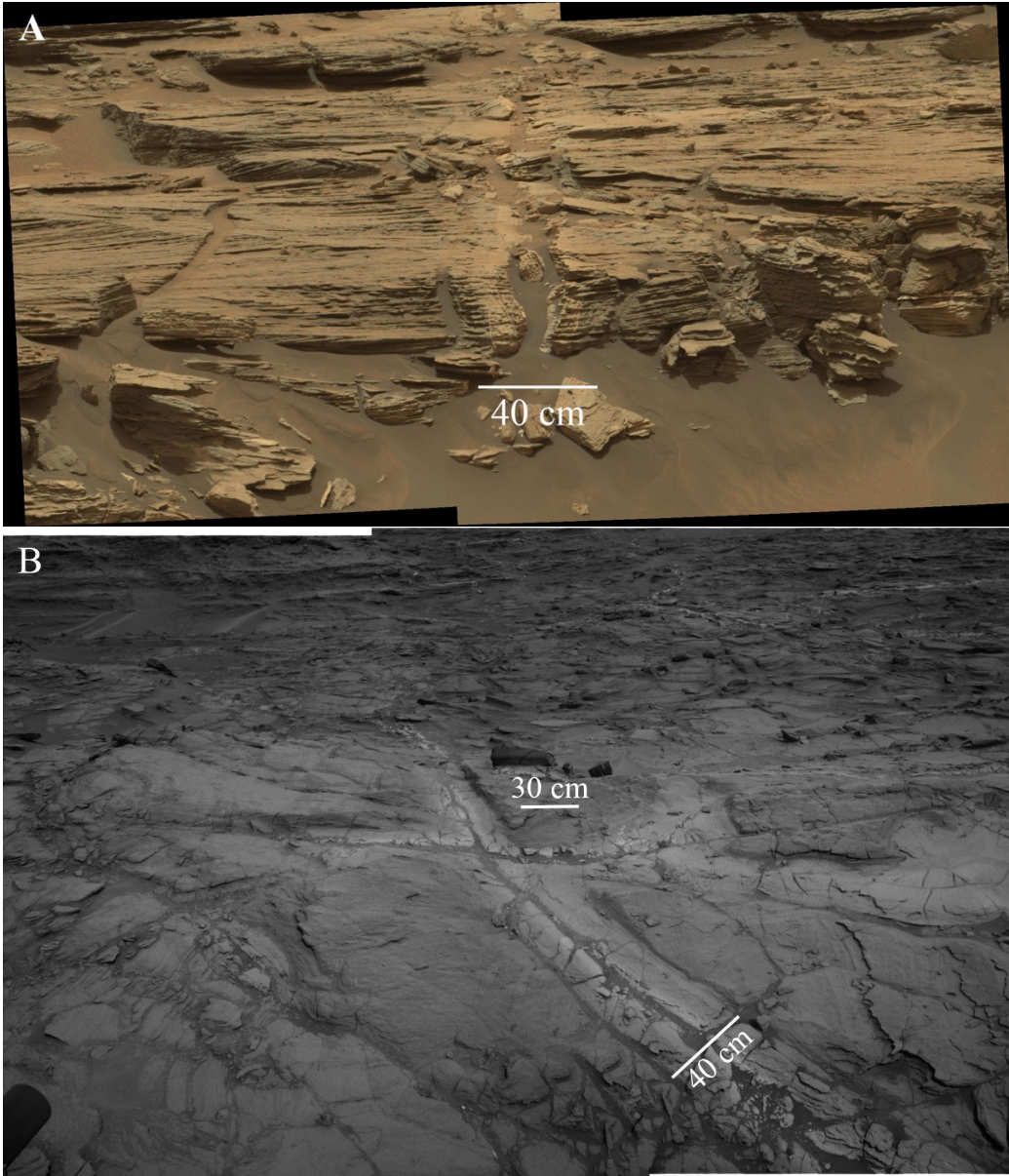


Figure S2: Light-toned fracture-associated diagenetic halos observed in darker-toned Stimson bedrock. The fractures and halos cut across bedding. A) Mastcam-100 sol 993 mosaic of images 0993MR0043950670503249C00 and 0993MR0043950680503250C00 at Marias Pass. B) Navcam left B-camera mosaic acquired with sequence ncam00835 on sol 1083 during the traverse to Bridger Basin.

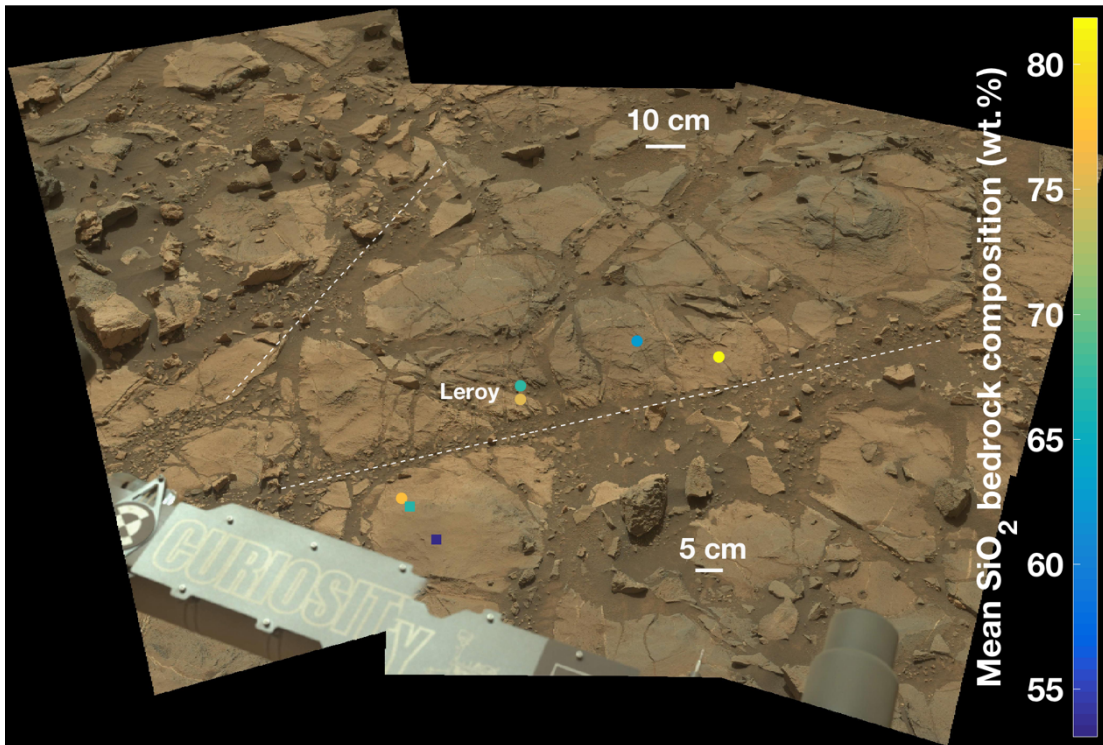


Figure S3: Mastcam-34 mosaic from sol 1108 (sequence mcam04927) showing fracture-related diagenetic halos observed in Murray bedrock at Bridger Basin. Locations of ChemCam (circles) and APXS (squares) measurements are annotated and color-coded per the mean bedrock composition measured. The ChemCam Leroy target raster crosses between halo and baseline Murray and is split into two points. Dashed lines indicate the approximate center-lines of halos.

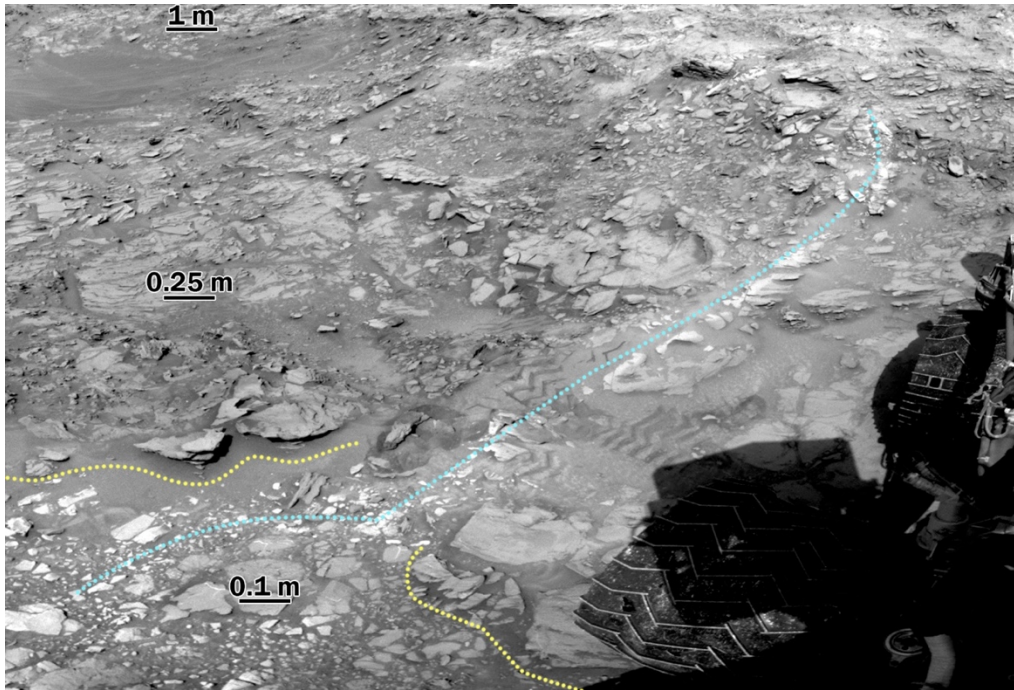


Figure S4: Part of Navcam left B-camera mosaic acquired on sol 1108 (contrast has been stretched, gamma correction). View is facing east, down to the right of the rover. Yellow traces indicate the contact between Stimson (top right) and underlying Murray (bottom left). Light blue trace shows the trend of the fracture-associated halo, indicating that it crosses the contact between the Murray formation and overlying Stimson formation.

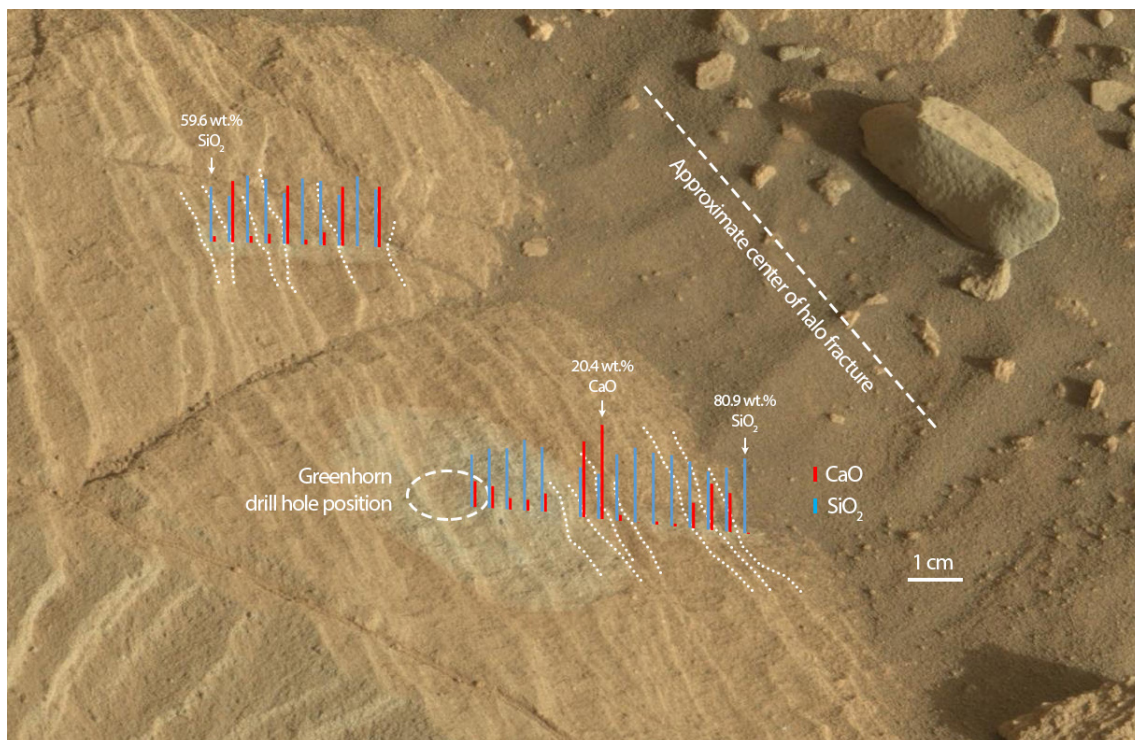


Figure S5: Locations of the individual ChemCam observation points of the targets Greenhorn, Greenhorn_2, and Benchmark near the Greenhorn drill hole (approximate location indicated by dashed ellipse) are annotated by colored bars. The blue bars represent the ChemCam SiO₂ content for each point. The SiO₂ content drops on a cm-scale moving radially away from the center of the fracture. The red bars represent the CaO content of each point. Almost 50% of the points in each raster show elevated CaO, most likely in the form of Ca-sulfates, corresponding to the lighter-toned veins and layers in the bedrock. These high-CaO points are not included as ChemCam bedrock points, yet are represented in the APXS 1.7 cm diameter surface observation. The image is a cropped version of a Mascam-100 mosaic acquired of the Greenhorn drill site (sequence: mcam05066) on sol 1134.

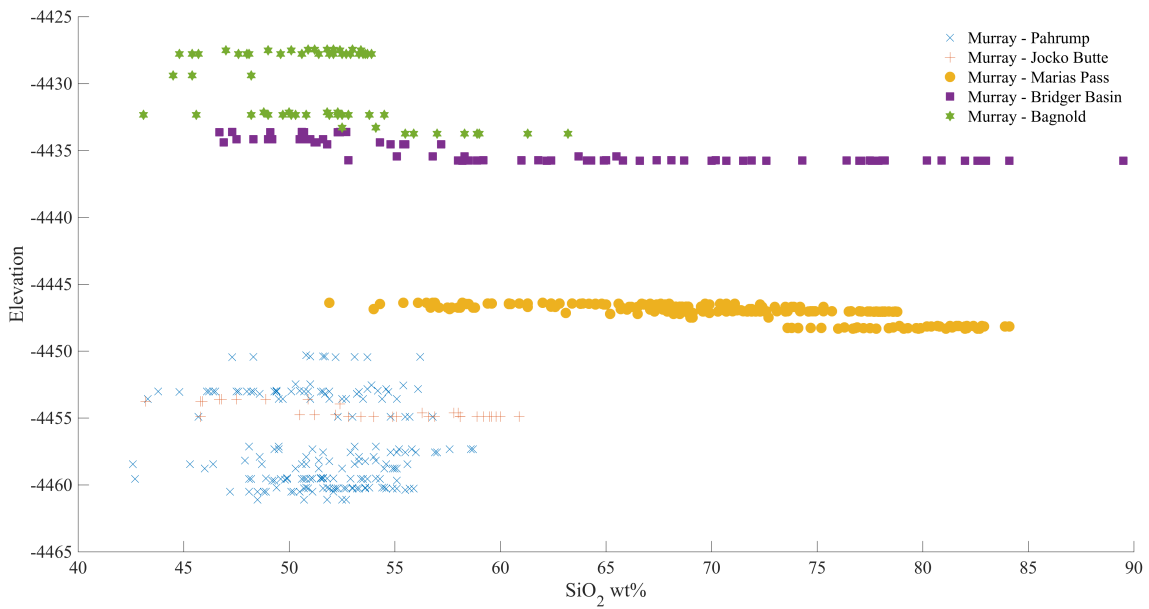


Figure S6: The SiO₂ content in Murray bedrock as measured by ChemCam vs. elevation. The high silica observed in the Murray formation at Marias Pass and Bridger Basin clearly stands out relative to the observations acquired at lower elevations (the Pahrump Hills and Jocko Butte locations) and at higher elevations south of Bridger Basin (here, the Bagnold area). The Murray formation bedrock observed when the rover first arrived at the Bridger Basin location shows a silica composition comparable to that observed south of Bridger Basin subsequently. The elevated silica at Bridger Basin was only observed after descending an additional 2 m.

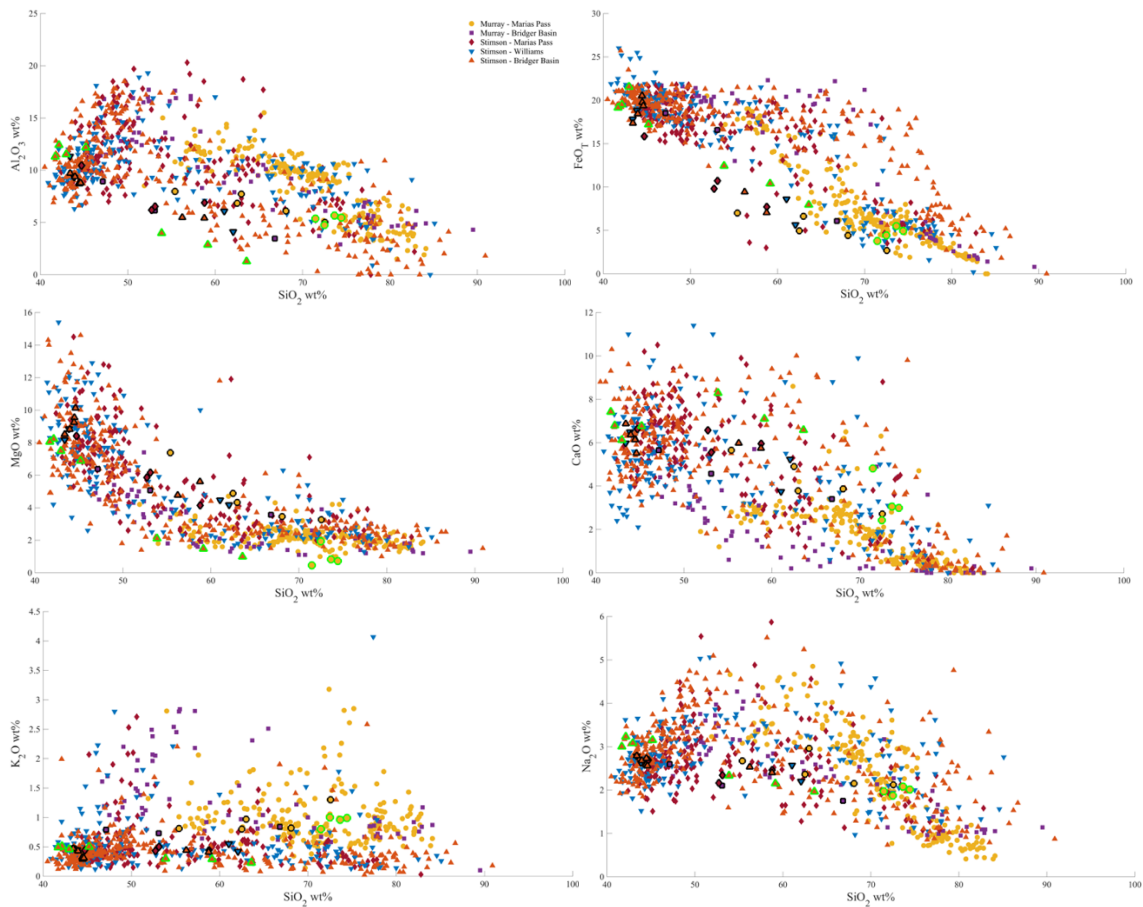


Figure S7: Plots showing the relative change in major-element content relative to increasing SiO₂ for all of the ChemCam and APXS observations performed; filled symbols with no edges are ChemCam measurements, symbols with green edges indicate APXS drill cuttings observations, and black edges indicate all other APXS observations. Apart from K₂O, all major elements plotted are seen to decrease with increasing silica. K₂O is constant in the Murray formation across all silica compositions, while it is mostly at the ChemCam level of quantification in the Stimson formation observations. Overall, a good agreement between APXS and ChemCam is observed. The primary causes for the observed differences is most likely the inclusion of Ca sulfate veins and/or intergranular cements within the APXS field of view, as observations of veins by ChemCam are not included here. This is consistent with CaO typically being higher in the APXS measurements. As APXS normalizes to 100%, the inclusion of Ca-sulfate in the APXS field-of-view cause a relative decrease of other major elements relative to CaO; this is consistent with other APXS measurements tending to be low relative to the ChemCam measurements.

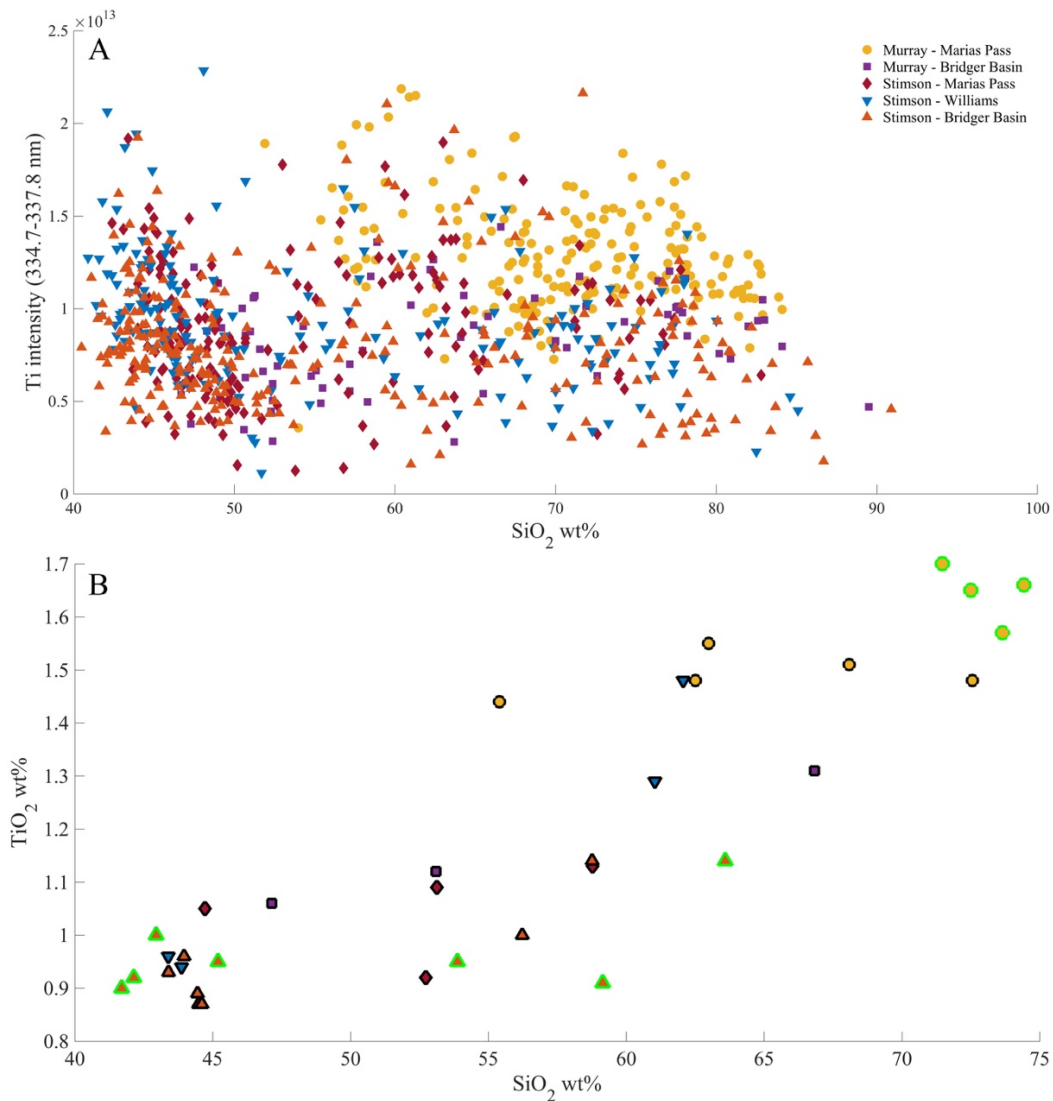


Figure S8: A) Total intensity of the three diagnostic Ti spectral lines between 334.7 and 337.8 nm plotted against SiO₂ wt.% as measured by ChemCam, B) TiO₂ wt.% versus SiO₂ wt.% as measured by APXS. Points with green edges indicate drill fines observations, black edges indicate all other APXS observations. Both the Ti line intensity and APXS TiO₂ measurement indicate that although the TiO₂ content is seen to increase with SiO₂ overall, the TiO₂ content remains approximately constant with increasing silica within each group. The Murray formation rocks at Marias Pass have a higher Ti-content than the other groups.

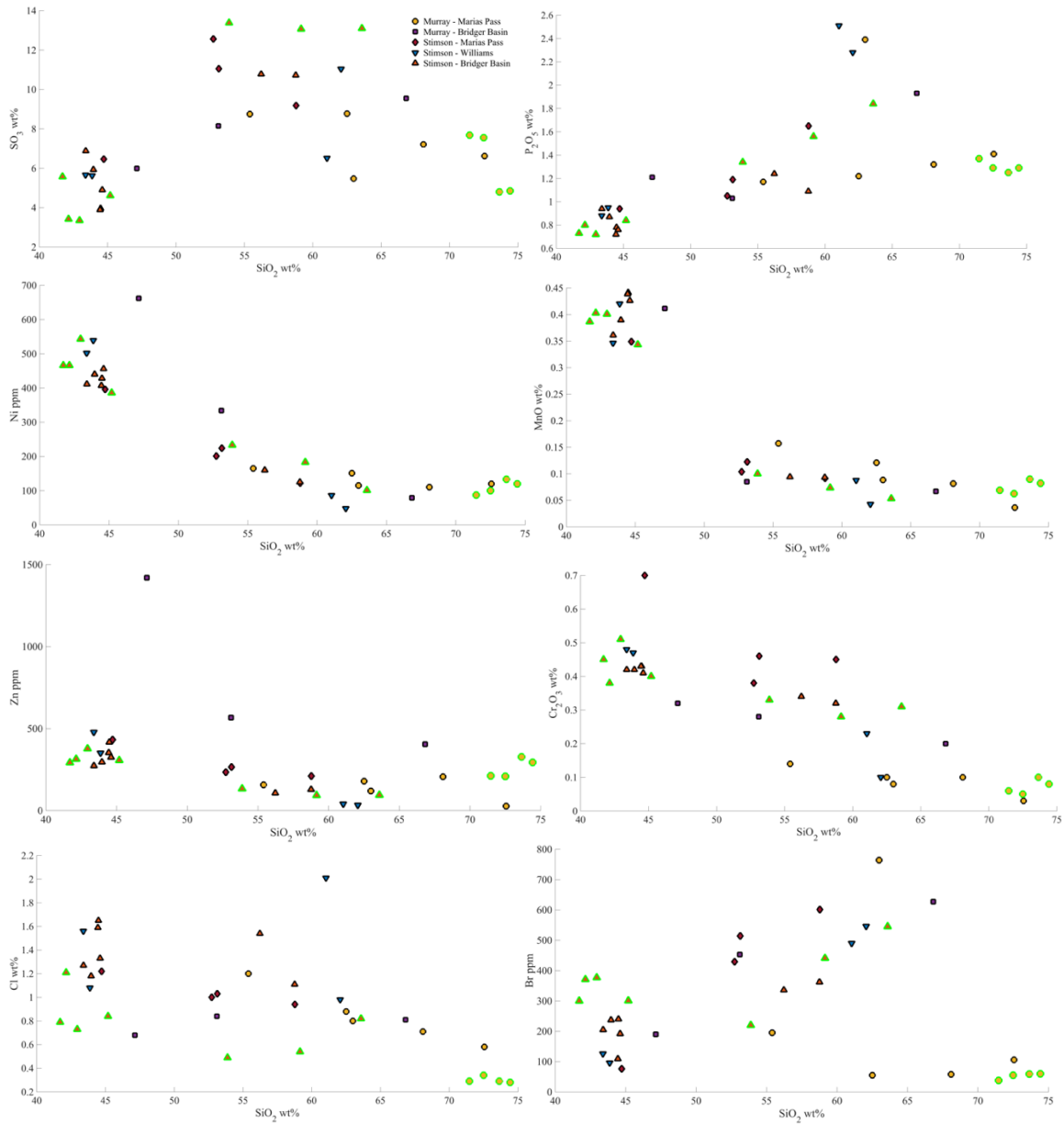


Figure S9: Minor element compositions measured by APXS only. While substantial scatter is observed (e.g., for Br), element abundances generally decrease with increasing SiO₂ like that observed for the major elements, with the notable exception of SO₃ and P₂O₅ which show an increase in the Stimson groups (top panels, left and right). Points with green edges indicate drill cuttings observations, black edges indicate all other APXS observations.

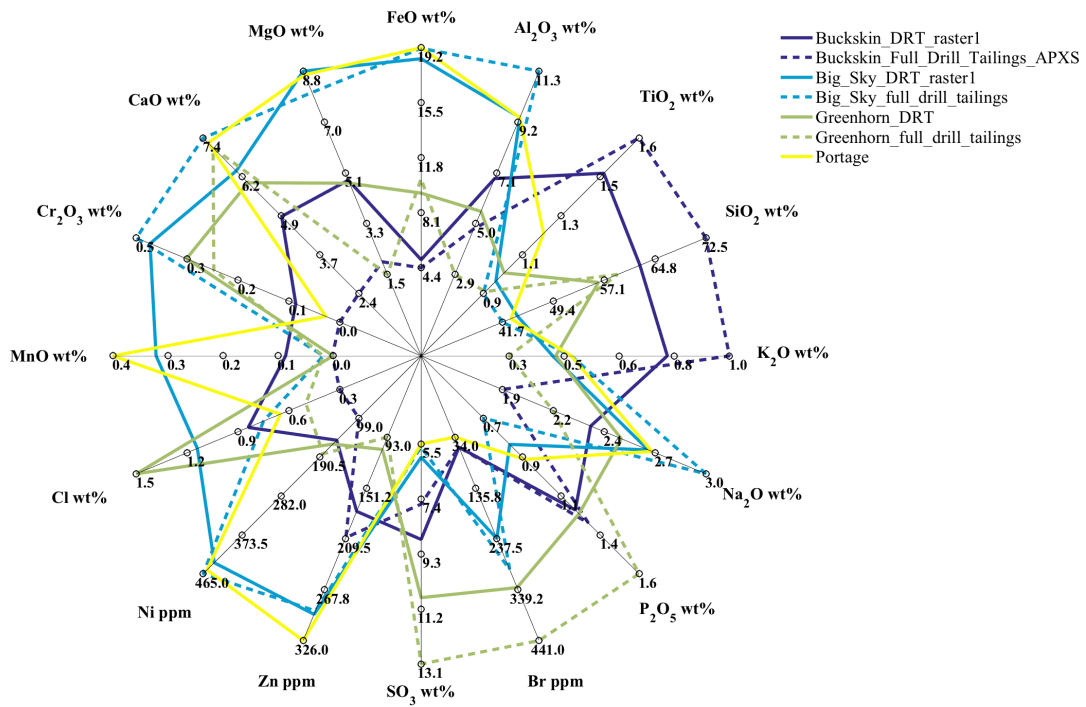


Figure S10: Spider plot of all the oxides quantified by APXS; note that each axis is scaled to the minimum and maximum of the measurements plotted. APXS measurements from the three drill samples collected at Marias Pass and Bridger Basin are plotted along with the Portage measurement, to illustrate a typical Mars soil composition (solid yellow line). Solid lines represent the pre-drill brushed bedrock observation, and the dashed lines represent the post-drill observation of the fresh drill cuttings. Except for CaO in the Greenhorn drill cuttings (in which subsurface calcium sulfate veins were sampled), a trend towards the soil composition is observed for all major elements, in particular for silica and magnesium. That is, the solid lines are always between the dashed lines of the same color and the Portage soil composition (yellow line). This suggests that dust has a notable effect for APXS measurements even on brushed targets.